




Emergence of topological states in a hybrid superconductor of monolayer Pb grown on NbSe₂Ze Huang ¹, Zhenyu Zhang ^{1,2} and Ping Cui ^{1,2,*}¹*International Center for Quantum Design of Functional Materials (ICQD), Hefei National Research Center for Physical Sciences at the Microscale, University of Science and Technology of China, Hefei, Anhui 230026, China*²*Hefei National Laboratory, University of Science and Technology of China, Hefei, Anhui 230088, China*

(Received 22 July 2023; revised 13 May 2024; accepted 12 June 2024; published 24 June 2024)

Topological superconductors have attracted tremendous interest in recent years because of their fundamental importance and potential applications in topological quantum computing. Here, using a monolayered Pb(111) film grown on a NbSe₂ substrate as an example, we show that it is possible to render a hybrid superconducting system nontrivial topology by combining two conventional *s*-wave superconductors with sufficiently strong spin-orbit coupling (SOC). We first demonstrate, based on first-principles calculations, that the monolayered Pb(111) film is stable on NbSe₂, and the system possesses a nonzero Z_2 topological invariant as well as Dirac-like edge states. Such a nontrivial topology originates from hybridization of the Pb and NbSe₂ bands, associated with a gap closure and reopening process in the presence of SOC. We further reveal that the (3×3) -type charge density wave (CDW) on the NbSe₂ surface is converted into a (2×2) -type CDW for the heterosystem, and the nontrivial topology is inherited in the CDW phase. Moreover, the CDW phase is still superconducting, albeit with a reduced transition temperature, exhibiting delicate competitions between the CDW and superconducting orders. Our findings offer opportunities for realizing topological superconductivity based on conventional *s*-wave superconductors.

DOI: [10.1103/PhysRevB.109.224516](https://doi.org/10.1103/PhysRevB.109.224516)**I. INTRODUCTION**

Topological superconductors have gained considerable interest in recent years, owing to their ability to host non-Abelian Majorana fermions that can serve as the building blocks for robust quantum computation [1–3]. Read and Green [4] demonstrated that a two-dimensional (2D) chiral *p*-wave superconductor is topologically nontrivial and can harbor Majorana edge modes. Limited candidate systems have been reported to be intrinsic chiral *p*-wave superconductors to realize topological superconductivity (TSC), such as Sr₂RuO₄ [5,6], Pb₃Bi [7], UTe₂ [8], and graphene-based systems [9–12]. Fu and Kane [13] proposed that, in a topological insulator/*s*-wave superconductor heterostructure, topological surface states coupled with superconducting states via the real-space proximity effect can mimic an effective 2D chiral *p*-wave superconductivity. Motivated by this idea, several topological insulator/superconductor heterostructures have been fabricated with the coexistence of superconductivity and topological order [14–17], and signatures of Majorana modes have also been observed in Bi₂Te₃/NbSe₂ heterostructures [18]. A drawback of this scheme is that the superconducting gap exhibits an exponential decay with the increasing thickness of the topological insulator. An alternative scheme for realizing TSC is to integrate Dirac-type surface states and superconductivity in a single material, where the two essential ingredients of TSC are coupled via the reciprocal-space proximity effect. Representative examples include metal-doped topological insulators [19–21] and Te-doped FeSe supercon-

ductors [22–28], yet in these systems, doping may lead to unavoidable stoichiometric inhomogeneities. Some noncentrosymmetric superconductors or 2D superconductors that possess nontrivial band topology have also been predicted to realize TSC via the reciprocal-space proximity effect [29–45], but the nontrivial topology in the superconducting regime remains to be proven definitively. Given these challenges encountered in various materials invoking different approaches, it is still highly desirable to discover materials that can serve as promising platforms for realizing TSC and exploiting braiding of the Majorana fermions for quantum computing.

Among the three conceptual schemes to achieve TSC—i.e., intrinsic chiral *p*-wave superconductors, enabled by the real-space proximity effect, and enabled by the reciprocal-space proximity effect [46]—the last one has been proven to be more advantageous for material diversity. One effective way to couple superconductivity and nontrivial topology via the reciprocal-space proximity effect is directly driving an *s*-wave superconductor into a topologically nontrivial phase. Given the vital role of spin-orbit coupling (SOC) in inducing nontrivial band topology [47–49], it is conceivable to cause a topological phase transition when proximity coupling a system with inherently large SOC to an *s*-wave superconductor. Meanwhile, to preserve the superconductivity of the combined system, a naturally more desirable choice for the large-SOC system is another superconductor as well. With these considerations, it is appealing to construct a heterostructure consisting of two conventional *s*-wave superconductors with considerably strong SOC to realize TSC via the reciprocal-space proximity effect.

Given the above design rationale, we take a monolayered Pb(111) film possessing large SOC [50,51] and

*Contact author: cuipeg@ustc.edu.cn

superconductivity [52,53], grown on an extensively studied superconductor substrate NbSe₂, as the concrete example in this paper. Using first-principles approaches, we identify that Pb(111)/NbSe₂, each component as a trivial (*s*-wave) superconductor yet as a combined system, harbors both superconductivity and nontrivial band topology as well as intriguing competing orders. First, the system is shown to be thermodynamically stable at room temperature and develops a nontrivial band topology, as characterized by a nonzero Z_2 topological invariant as well as Dirac-like edge states. The topologically nontrivial property arises from the distinct band hybridization between the Pb overlayer and NbSe₂ substrate, exhibiting a gap closure and reopening process with increasing SOC, which can be explained within the Kane-Mele model [48]. Next, we reveal the existence of a charge density wave (CDW) instability in this heterosystem at low temperatures and identify a 2×2 CDW ground state, which is different from the (3×3) -type CDW phase of NbSe₂. The nontrivial topological properties can still be inherited in this CDW phase. Furthermore, we study the superconducting property of both the normal (non-CDW) and CDW phases, showing their preserved superconducting nature, and reveal the competitive interactions between the CDW and superconducting orders in this system. Collectively, the central findings expand the candidate materials for achieving coexistence of superconductivity and nontrivial band topology and offer opportunities for realizing TSC based on *s*-wave superconductors.

This paper is organized as follows. In Sec. II, we briefly describe the computational methods and details. In Sec. III, we first study the atomic configurations, stability, and electronic properties of the Pb(111)/NbSe₂ system and reveal the nontrivial band topology. We then investigate the superconducting and CDW properties and discuss their coexistence and competition. Furthermore, we provide a discussion and perspective on the realization of TSC and Majorana zero modes. Finally, we summarize in Sec. IV.

II. COMPUTATIONAL METHODS

We have employed VASP [54,55] for structural optimization, electronic property calculations, and *ab initio* molecular dynamics (AIMD) simulations based on density functional theory (DFT), where the projector augmented-wave [56,57] method was adopted, and the generalized gradient approximation (GGA) in the framework of Perdew-Burke-Ernzerhof (PBE) [58] was chosen for the exchange-correlation functional. The plane-wave cutoff energy was set to 500 eV for all calculations. When simulating the Pb(111)/NbSe₂ system, the semi-infinite NbSe₂ substrate was modeled using a slab consisting of four monolayers of NbSe₂ with the bottommost two monolayers fixed to their bulk positions. A vacuum layer was set to be $>15 \text{ \AA}$ to ensure decoupling between neighboring slab images. A (1×1) surface unit cell and a $15 \times 15 \times 1$ k -point mesh were used during structural optimization and electronic property calculations. During the relaxation, except for the bottommost two NbSe₂ monolayers, all atoms were allowed to relax until the residual forces on each atom were $<0.01 \text{ eV/\AA}$. When using finite-temperature AIMD simulations to test the thermodynamic stability, a (3×3) surface

supercell and a $3 \times 3 \times 1$ k -point mesh were used. A canonical ensemble was adopted for the AIMD simulations using the algorithm of Nosé [59], with a time step of 2 fs. The Z_2 invariants were calculated via the Wannier charge center method [60], and the edge Green's functions [61] were obtained by using the maximally localized Wannier functions [62] as implemented in the WANNIERTOOLS package [63]. In the wannierization process, we used the Nb-*d*, Se-*p*, and Pb-*p* orbitals for the initial projections and obtained the well-localized Wannier functions that correctly reproduce the DFT-calculated band structures.

The NbSe₂ substrate has a layered structure with three atomic layers as a monolayer, and neighboring monolayers are coupled through van der Waals (vdW) interactions. To describe the interlayer interactions more accurately, we examined four different vdW correction schemes beyond the GGA: two semiempirical schemes (DFT-D2 [64] and DFT-D3 [65]) and two methods using nonlocal correlation functionals in treating the dispersion interactions (vdW-DF2 [66] and optB88-vdW [67]). As a benchmark test, we calculated the lattice constants of bulk NbSe₂ using the four vdW correction schemes. It was found that the DFT-D3 method yields the optimal lattice constants of $a = b = 3.446 \text{ \AA}$ and $c = 12.370 \text{ \AA}$, in good agreement with the experimental values ($a = b = 3.443 \text{ \AA}$ and $c = 12.547 \text{ \AA}$) [68]. Therefore, the DFT-D3 method was used in all calculations.

Phonon dispersions were calculated using the density functional perturbation theory (DFPT) coded in the QUANTUM ESPRESSO package [69], with optimized norm-conserving Vanderbilt pseudopotentials [70] and a 90 Ry energy cutoff of the plane-wave basis. To probe the superconductivity of the heterosystem, we consider a slab model consisting of one Pb monolayer and one NbSe₂ monolayer. Here, we used a $9 \times 9 \times 1$ k -point grid for the structural optimization of the CDW-modulated structures, and the geometries were optimized until the residual atomic forces were $<1 \times 10^{-4}$ Ry/Bohr. For the normal phase, the phonon dispersion was obtained by Fourier interpolation of the dynamical matrices computed on an $18 \times 18 \times 1$ k mesh and a $9 \times 9 \times 1$ q mesh. For the 2×2 CDW phase, the Brillouin zones (BZs) for electronic and vibrational calculations were sampled using $9 \times 9 \times 1$ and $3 \times 3 \times 1$, respectively. The Migdal-Eliashberg mechanism was employed to calculate the transition temperature as implemented in the EPW code [71,72], and the interpolated k -point grid of $192 \times 192 \times 1$ ($90 \times 90 \times 1$) and q -point grid of $96 \times 96 \times 1$ ($30 \times 30 \times 1$) were used to calculate the superconducting properties of the normal phase (CDW phase). If there existed small imaginary frequencies near the Γ point in the phonon spectra, we excluded phonons with frequencies $<5 \text{ cm}^{-1}$ in calculating the electron-phonon coupling (EPC) matrix elements, to guarantee that the corresponding carrier scattering was physically meaningful.

III. RESULTS AND DISCUSSION

A. Atomic configurations and stability

To investigate whether a monolayered Pb(111) film can be grown on a NbSe₂ substrate, we first investigate the energetics of different stacking configurations. Given the relatively small

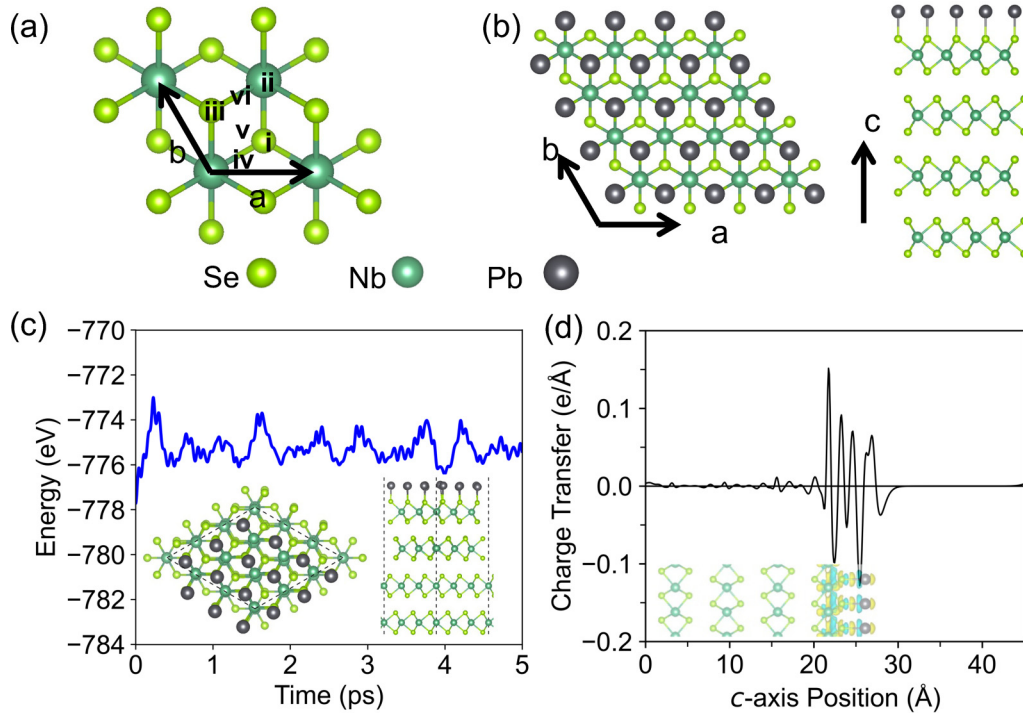


FIG. 1. (a) High- and low-symmetry adsorption sites on NbSe₂. The high-symmetry top, hcp, and fcc sites are labeled by (i), (ii), and (iii), respectively. The low-symmetry bridge I, II, and III sites are labeled by (iv), (v), and (vi), respectively. (b) Top (left panel) and side (right panel) views of the top configuration of Pb(111)/NbSe₂. (c) Evolution of the total energy of the configuration during a 5 ps *ab initio* molecular dynamics (AIMD) simulation at 300 K. The insets show the top and side views of the structure after the 5 ps AIMD simulation. (d) Plane-averaged charge density difference of the top configuration along the *c* axis. The inset denotes the atomic structure superimposed with the spatial distribution of charge density difference. The blue and yellow regions indicate electron depletion and accumulation, respectively.

lattice mismatch between the in-plane constants of Pb(111) and NbSe₂ (2.44%), a 1×1 surface unit cell was used for the combined system. The initial configurations with one Pb atom sitting on three high-symmetry adsorption sites (labeled as fcc, hcp, and top) or three low-symmetry adsorption sites (labeled as bridges I, II, and III) are considered, as shown in Fig. 1(a). Upon relaxation, we obtain three configurations, where the top configuration [see Fig. 1(b)] is energetically much more stable than the fcc and hcp ones, with the total energy lower by 0.244 and 0.320 eV per unit cell, respectively. In the following study, we focus on this most stable configuration. To examine the thermodynamic stability of the top configuration, we also perform the AIMD simulations at 300 K. The results are contrasted in Fig. 1(c), revealing that the Pb overlayer essentially preserves its ordered structure after a 5 ps AIMD simulation. Based on these results, we can conclude that a monolayered Pb(111) film is highly probable to be fabricated on the NbSe₂ substrate, and the system is stable at room temperature.

In the top configuration, the calculated distance between the Pb and topmost Se atoms is ~ 2.81 Å, distinctly shorter than that in bulk PbSe (3.103 Å) [73], indicating that the interaction between the Pb overlayer and NbSe₂ is not vdW type but with chemical bonds formed. In contrast, the Pb-Se distances in the hcp and fcc configurations are 3.31 and 3.27 Å, respectively, suggesting the vdW nature of the interaction between the Pb overlayer and NbSe₂. The bonding strength between Pb and Se can also be reflected by the charge density difference of the system, calculated by the total charge density of Pb(111)/NbSe₂ subtracting the charge density of

the Pb(111) overlayer and that of the bare NbSe₂ substrate. As shown in Fig. 1(d), there is a significant charge transfer of ~ 0.57 electrons per Pb from the overlayer to substrate, confirming the strong interlayer interaction. Qualitatively, the charge transfer can be understood from the smaller electronegativity of Pb than that of Se and the larger work function of the NbSe₂ substrate (5.6 eV) than that of the Pb monolayer (4.3 eV). We also observe that the hybridization between Pb and the substrate is concentrated on the top-layer NbSe₂, as characterized by negligible charge density difference in the rest of the NbSe₂ layers. Such an interaction may result in a relatively strong band hybridization between Pb and the top-layer NbSe₂ and drive the system into a topologically non-trivial phase with inherently strong SOC of Pb, as discussed in the next subsection.

B. Electronic band structures

Figures 2(a) and 2(b) display the band structures of the top configuration of Pb(111)/NbSe₂ calculated without and with SOC, respectively, both with the projections onto the Nb-*d*, Se-*p*, and Pb-*p* orbitals. To explore the effect of Pb on the electronic structure of the NbSe₂ substrate, we first calculate the band structures of a four-layer NbSe₂, as shown in Fig. S1 in the Supplemental Material [74]. Without SOC, the system exhibits a metallic nature, with the Nb-*d* orbitals dominating around the Fermi level and the Se-*p* states mainly located below -0.6 eV. When SOC is included, some of the degenerate points are opened (for example, the Nb-*d* orbitals

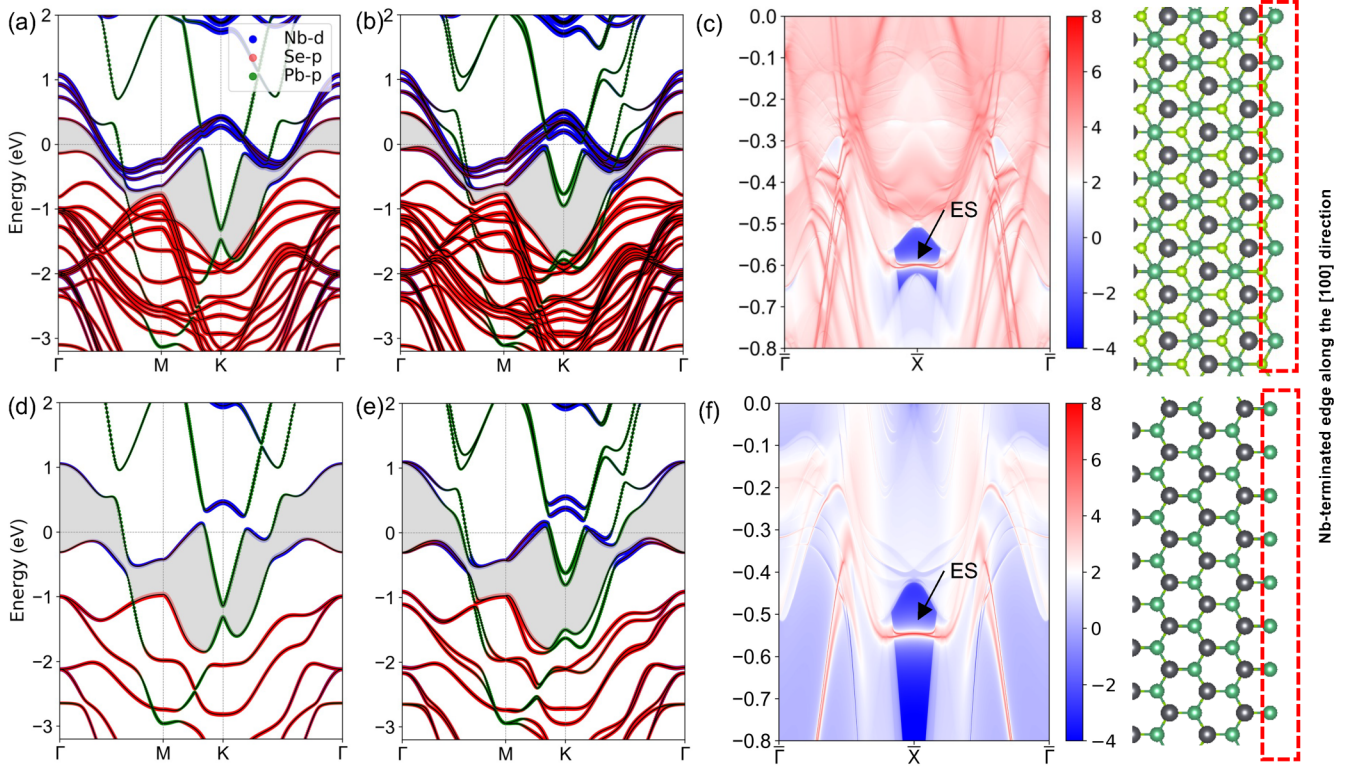


FIG. 2. Band structures of Pb(111)/NbSe₂ (a) without and (b) with spin-orbit coupling (SOC). The Fermi levels are all set at zero, and the continuous energy gaps in the whole Brillouin zone are highlighted by the gray shaded regions. The blue, red, and green data points denote the spectral weights contributed by the Nb-*d*, Se-*p*, and Pb-*p* orbitals, respectively. (c) Edge states (ESs; left panel) and configuration (right panel) of a semi-infinite slab along the [100] direction. The warmer colors denote higher local density of states, and the blue regions denote the bulk band gaps. (d)–(f) Same as (a)–(c) but for the heterobilayer.

at the *K* point), but the spin degeneracy of all bands is still protected by the coexistence of the time-reversal and inversion symmetries. Once depositing the Pb(111) overlayer, as shown in Fig. 2(a), the metallic nature is preserved, and the Pb-*p* bands are also present around the Fermi level. These Pb-*p* bands are highly dispersive and strongly hybridize with the Nb-*d* and Se-*p* bands, leading to complicated band orders. Such significant band hybridizations are consistent with the considerable charge transfer as well as the chemical bonding between Pb and Se presented above. At the *K* point, the Dirac-type band dispersion of Pb is gapped out due to the effect of the substrate (i.e., the built-in electric field formed at the interface due to the charge transfer), which results in a continuous gap throughout the whole BZ [the gray areas in Fig. 2(a)]. When SOC is turned on, as shown in Fig. 2(b), the band structure exhibits giant Rashba splitting within the whole BZ except at the high-symmetry points protected by time-reversal symmetry (i.e., the Γ and *M* points), which is attributed to the breaking of spatial inversion symmetry and the strong SOC effect of the Pb atoms. Aside from the band splitting, the gap of the Dirac-type Pb-*p* bands at the *K* point increases significantly in the presence of the SOC, which indeed corresponds to a gap closure and reopening process with increasing SOC, as elaborated later.

C. Topological properties

Given the above analysis on the band structures and the strong SOC introduced by Pb, we now explore the topological

properties of the Pb(111)/NbSe₂ system by evaluating the topological invariant Z_2 that classifies the topological properties of time-reversal invariant systems. Although the system has no global gap, we can separate the bands into occupied and unoccupied states by assuming a curved chemical potential in the continuous gap through the whole BZ [23]. Here, the minimum energy difference value along this continuous gap is calculated to be ~ 0.073 eV using a dense Monkhorst-Pack *k*-point grid of $41 \times 41 \times 1$. The corresponding Z_2 invariant can be determined by the occupied states using the hybrid Wannier function method [60]. As shown in Fig. 2(b), a curved chemical potential can be identified in the continuous gap highlighted in gray and yields a nonzero Z_2 number (see Fig. S2(a) in the Supplemental Material [74]), indicating the nontrivial topology of the system. Another manifestation of the nontrivial topology in the band structures is the existence of robust gapless boundary states located inside the bulk band gap. For the heterostructure system of monolayered Pb(111) on four-layer NbSe₂, we then calculate the energy spectra of the edge of a semi-infinite slab along the [100] direction, clearly showing the Dirac cone-type states at the \bar{X} point, as displayed in Fig. 2(c). Here, we note that these topological edge states are located at 0.6 eV below the Fermi level, which can participate in the superconducting pairing via proper carrier doping or gating. Since there also exist multiple bands of Pb(111)/four-layer NbSe₂ in this energy window, it is expected to differentiate the topological edge states from these trivial states in experiments, as demonstrated

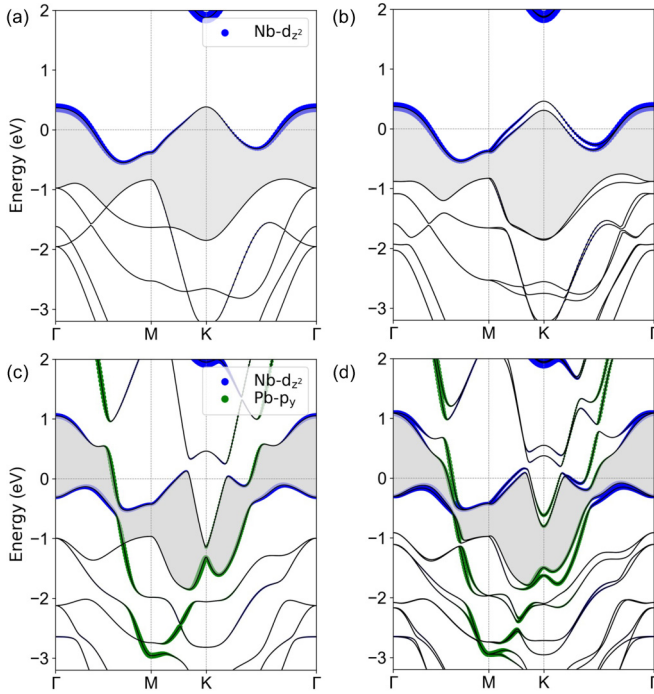


FIG. 3. Orbital-projected band structures of (a) and (b) a NbSe₂ monolayer and (c) and (d) the heterobilayer, calculated (a) and (c) without and (b) and (d) with spin-orbit coupling (SOC), respectively. The blue and green data points denote the spectral weights contributed by the Nb- d_{z^2} and Pb- p_y orbitals, respectively.

in some 2D systems using *in situ* scanning tunneling microscopy/spectroscopy measurements [41,75].

To get a deeper understanding of the origin of the nontrivial topology, we use a heterobilayer of monolayered Pb(111) on a NbSe₂ monolayer as a simplified system, which can largely reproduce the band characters of Pb(111)/NbSe₂ but with reduced band numbers. First, we confirm that the top configuration is the most stable stacking structure of the heterobilayer with the formation of the chemical bonding and is lower in energy by 0.247 and 0.330 eV per unit cell than the fcc and hcp ones, respectively. The corresponding band structures calculated without and with SOC are displayed in Figs. 2(d) and 2(e), showing similar band hybridization and curved gap features with that of the considered Pb(111)/NbSe₂ system above [see Figs. 2(a) and 2(b)]. The topological properties of the heterobilayer system are also confirmed by the nonzero Z_2 number (see Fig. S2(b) in the Supplemental Material [74]) and Dirac cone-type edge states [see Fig. 2(f)]. Collectively, the heterobilayer reproduces the structural, electronic, and topological properties of the above Pb(111)/NbSe₂ system, justifiable to explore the mechanism of the nontrivial topology.

Next, we analyze the detailed band structures of the heterobilayer and examine the effect of SOC by controllably altering the SOC strength. Like the Pb(111)/NbSe₂ system [see Figs. 2(a) and 2(b)], the strong hybridization between the Pb- p and Nb- d /Se- p bands leads to complicated band orders around the Fermi level. For example, by comparing the band structures of a NbSe₂ monolayer and the heterobilayer (see Fig. 3), we observe that part of the Nb- d_{z^2} band is inverted

from the valence band to the conduction band with respect to the continuous gap (the gray area) at the Γ point, and the newly introduced Pb- p_y band appears below the continuous gap at the M point. Such complicated band orders at the high-symmetry points result in a topological phase transition, as confirmed by $Z_2 = 1$. It is worthwhile to point out that, in contrast with most topological insulators [49,76], the presence of SOC does not induce any additional band order change between the valence and conduction bands in the whole BZ (see Fig. S3 in the Supplemental Material [74]). Nevertheless, only when SOC is included, the calculated $Z_2 = 1$, implying the indispensable role of SOC on the band topology.

To elucidate the impact of SOC in the topological phase transition process, we manually vary the SOC strength (T_{SO}) from zero to the actual SOC strength value of the system (T_{real}) and examine the band structure and Z_2 invariant of the heterobilayer. The results are shown in Figs. 4(a)–4(g) and Fig. S4 in the Supplemental Material [74]. Here, $T_{SO} = 0$ means that SOC is not considered, and $0 < T_{SO}/T_{real} < 1$ correspond to some artificial cases. Strikingly, we observe a gap closing and reopening for the Dirac-type dispersion of the Pb bands at the K point with increasing T_{SO} [see the gray areas in Figs. 4(a)–4(f)], and the magnitude of the gap (E_{gap}) varies linearly with T_{SO} [see Fig. 4(g)]. The system is topologically trivial ($Z_2 = 0$) before the gap closes with $T_{SO}/T_{real} \leq 0.2$ and is nontrivial ($Z_2 = 1$) after the gap reopens with $T_{SO}/T_{real} > 0.2$ [see Fig. 4(g)]. These features are very similar to those in the Kane-Mele model for graphene [41,47]. In this model, the bands of graphene are already inverted at the M point in the absence of SOC, associated with parity exchanges of the valence and conduction bands, and the energy gap at the K point can be approximately expressed as $|6\sqrt{3}\lambda_{SO} - \lambda_v|$, linear with λ_{SO} . Here, λ_{SO} and λ_v are the strength of the SOC and the staggered sublattice effect of graphene, respectively. Graphene is trivial when the gap is dominated by λ_v , while the system becomes nontrivial when the SOC is large enough to close and reopen the gap. In our system, the interaction with NbSe₂ makes the Pb overlayer open the Dirac-type gap at the M point, characterizing the effect of λ_v . We also calculate E_{gap} with increasing distance between Pb and NbSe₂ (d_{Pb-Se}) without the SOC and confirm that E_{gap} decreases with increasing d_{Pb-Se} and becomes zero when $d_{Pb-Se} > 4.6 \text{ \AA}$, as shown in Fig. 4(h). Based on these analyses, the Pb(111)/NbSe₂ systems share a similar mechanism toward topologicalization with the Kane-Mele model for graphene.

D. Superconducting properties

With the nontrivial topology established in Pb(111)/NbSe₂, we now need to examine whether the superconductivity of the system can be preserved. Because the calculations of the EPC of a Pb(111) overlayer on four-layer NbSe₂ are very demanding, here, we also use the Pb(111)/NbSe₂ heterobilayer to investigate the superconducting properties, given the similar justifications mentioned in the last subsection. Since the strong hybridization between Pb and NbSe₂ lies between Pb and the topmost layer and decays rapidly for the rest layers, the heterobilayer should be able to capture the main superconducting features of Pb(111)/NbSe₂. We adopt a

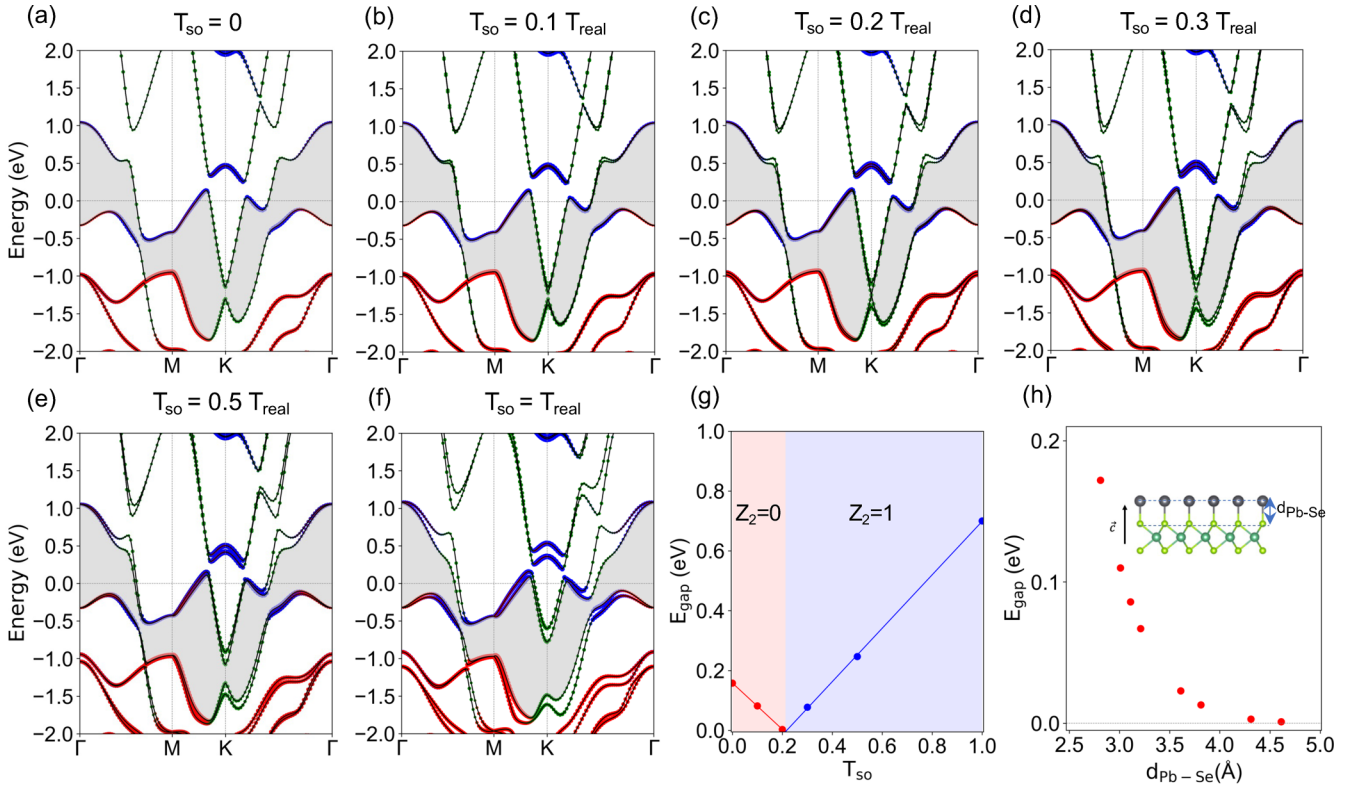


FIG. 4. (a)–(f) Band structures of the heterobilayer calculated with different spin-orbit coupling (SOC) strengths (T_{SO}). (g) Energy gap (E_{gap}) at the K point (in the gray shaded regions) as a function of T_{SO} , with the Z_2 invariant also indicated. The pink and purple regions denote $Z_2 = 0$ and 1, respectively. (h) E_{gap} as a function of the distance between Pb and NbSe₂ ($d_{\text{Pb-Se}}$; see the inset), calculated without SOC.

commonly used electronic broadening of $\sigma = 0.02$ Ry in the self-consistent calculations of the charge density to obtain the phonon dispersion of the heterobilayer. Here, the broadening corresponds to an electronic temperature of ~ 1500 K. It is worth noting that the temperatures estimated from the values of σ are usually about one order of magnitude larger than that in experiments, probably because the thermal motion of the ions is ignored in the DFPT calculations [77]. The phonon spectrum of the heterobilayer with the decomposition of atomic vibrations is shown in Fig. 5(b), and the soft phonons mainly originate from the vibration of the Pb atoms. As a comparison, we calculate the phonon spectrum of a freestanding NbSe₂ monolayer using the same σ , showing that the lowest phonon branch exhibits the minimum imaginary frequency at $\sim \frac{2}{3} \Gamma M$ [see Fig. 5(a)]. Such a feature implies a structural instability with 3×3 CDW modulations under this condition ($\sigma = 0.02$ Ry), which is consistent with the CDW transition temperature (T_{CDW}) of 145 K in the experiment [78]. In the presence of the Pb overlayer, the imaginary phonons are removed, indicating that the Pb overlayer helps to stabilize the NbSe₂ monolayer and suppress its CDW instability. The corresponding physical mechanism can simply be understood because of electron transfer, as demonstrated in a $1H$ -TaS₂ monolayer or a graphene/NbSe₂ heterostructure [79,80]. Note that the negligibly small imaginary frequencies near the Γ point correspond to the out-of-plane acoustic (ZA) mode, as shown in the Figs. 5(a)–5(d), and are caused by numerical

inaccuracies in calculating the interatomic forces [81,82], which is not a sign of structural transition.

The phonon density of states (PHDOS), the Eliashberg spectral function $\alpha^2 F(\omega)$, and the accumulative EPC $\lambda(\omega)$ of the heterobilayer are displayed in Figs. 5(f) and 5(g), where ω is the phonon frequency. The accumulative EPC $\lambda(\omega)$ can be obtained from $\alpha^2 F(\omega)$ by

$$\lambda(\omega) = 2 \int_0^\omega \frac{\alpha^2 F(\nu)}{\nu} d\nu. \quad (1)$$

The Eliashberg function $\alpha^2 F(\omega)$ is defined as

$$\alpha^2 F(\omega) = \frac{1}{2} \sum_{\nu} \int_{\text{BZ}} \frac{dq}{\Omega_{\text{BZ}}} \delta(\omega - \omega_{q\nu}) \omega_{q\nu} \lambda_{q\nu}, \quad (2)$$

where Ω_{BZ} is the volume of the phonon BZ, $\omega_{q\nu}$ is the phonon frequency for the phonon branch ν with the wave vector q , and $\lambda_{q\nu}$ is the ν - and q -resolved EPC parameter. The $\lambda_{q\nu}$ is given as

$$\lambda_{q\nu} = \frac{1}{N(\varepsilon_F) \omega_{q\nu}} \sum_{nm} \int_{\text{BZ}} \frac{d\mathbf{k}}{\Omega_{\text{BZ}}} \times |g_{mn,\nu}(\mathbf{k}, \mathbf{q})|^2 \delta(\varepsilon_{\mathbf{n}\mathbf{k}} - \varepsilon_F) \delta(\varepsilon_{\mathbf{m}\mathbf{k}+\mathbf{q}} - \varepsilon_F). \quad (3)$$

Here, $N(\varepsilon_F)$ is the density of states (DOS) at the Fermi level, $g_{mn,\nu}(\mathbf{k}, \mathbf{q})$ is the first-order electron-phonon matrix element, and the delta functions arise from energy conservation and reflect the nesting effect on the Fermi surface. Thus, we can

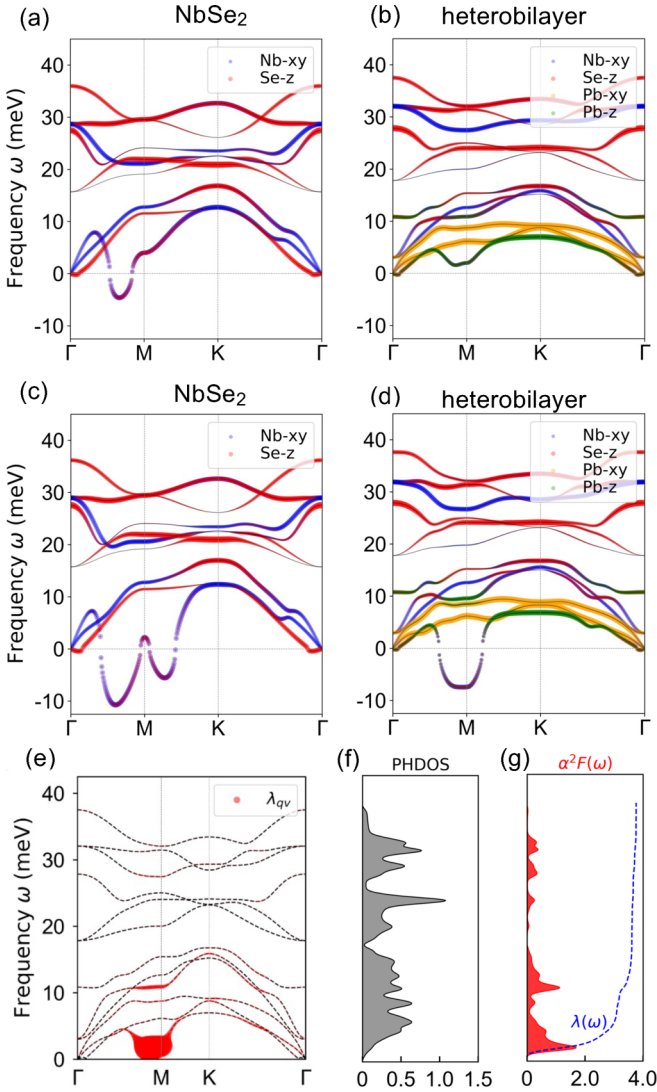


FIG. 5. Phonon spectra of (a) a NbSe₂ monolayer and (b) the heterobilayer, calculated using an electronic broadening of $\sigma = 0.02$ Ry. The blue, red, yellow, and green data points denote the spectral weights contributed by Nb in-plane, Se out-plane, Pb in-plane, and Pb out-plane vibration modes. (c) and (d) Same as (a) and (b) but for $\sigma = 0.01$ Ry. (e) Phonon spectrum of the heterobilayer with the magnitudes of λ_{qv} indicated by the data sizes in red. (f) and (g) The corresponding phonon density of states (PHDOS), Eliashberg function $\alpha^2 F(\omega)$, and accumulative electron-phonon coupling $\lambda(\omega)$.

obtain the total EPC strength of λ by taking the upper bound ω to ∞ in Eq. (1).

To further estimate the superconducting transition temperature (T_c), we use the McMillian-Dynes parametrized equation [83,84]:

$$k_B T_c = \frac{\hbar \omega_{\log}}{1.2} \exp \left[-\frac{1.04(1 + \lambda)}{\lambda - \mu^*(1 + 0.62\lambda)} \right], \quad (4)$$

where ω_{\log} is the logarithmic average of the phonon frequencies, and μ^* is the effective Coulomb interaction parameter.

The ω_{\log} is given as

$$\omega_{\log} = \exp \left(\frac{2}{\lambda} \int_0^{\infty} d\omega \frac{\alpha^2 F(\omega)}{\omega} \ln \omega \right). \quad (5)$$

By taking $\mu^* = 0.10 - 0.14$, T_c is estimated to be 7.73–7.28 K, higher than that of a non-CDW NbSe₂ monolayer [30] and that of a monolayered Pb(111) film on Si(111) [85,86] using the same method with the same calculation precision. From the distribution of λ_{qv} visualized by the red dots in Fig. 5(e), we can see that the major contribution to the EPC comes from the dip phonons around the M point. It is noted that such an anomalous dip mode around the M point usually indicates a potential CDW transition with decreasing temperature, which will be discussed in the next subsection.

E. CDW phases

Considering that CDW phonons are sensitively related to the electronic broadening during numerical calculations, the dip phonons may be associated with a possible CDW instability when reducing σ [87,88]. We further calculate the phonon spectrum of the Pb(111)/NbSe₂ heterobilayer using a small electronic broadening of $\sigma = 0.01$ Ry, as presented in Fig. 5(d). A strongly softened phonon mode is observed and exhibits imaginary frequencies around the M point, clearly indicating a structural instability at low temperatures. The phonon spectrum of a NbSe₂ monolayer with $\sigma = 0.01$ Ry is also contrasted in Fig. 5(c), showing a stronger instability than that with $\sigma = 0.02$ Ry. A common feature of the two systems is that the most unstable phonon mode mainly involves the in-plane vibration of the Nb atoms. The difference is that the dip phonons in the heterobilayer are located around the M point, implying a structural instability with 2×2 CDW modulations, while the NbSe₂ monolayer is more likely to experience a 3×3 CDW transition.

To determine the equilibrium atomic structures of the CDW states for the heterobilayer, we construct several 2×2 superstructures with different atomic distortions and carry out structural optimizations. Finally, two distorted structures are obtained, both of which generate a triangular Nb trimer plus one Nb atom (there are four Nb atoms in one supercell), as shown in the insets of Fig. 6(a). When the Nb trimer is located on the hollow site of the Pb lattice, the structure is labeled as CDW-1, while the other structure is labeled as CDW-2, with the center of the Nb trimer on top of one Pb atom. The energies of the CDW-1 and CDW-2 structures are lower than that of the 1×1 normal phase by 4.9 and 11.5 meV per 2×2 supercell, respectively, indicating the stabilities of the 2×2 CDW phases. To reveal the formation mechanism of the CDW phases, we calculate the relative energy (ΔE) to that of the normal phase by continuously changing the atomic displacements in the Nb trimer (d_{Nb}). Here, d_{Nb} represents the varying distance of one Nb atom in the Nb trimer of CDW-1 or CDW-2 away from its position in the normal phase. During structural optimization, the Nb trimer is always fixed, and all the other atoms are fully relaxed. As shown in Fig. 6(a), one stable configuration is located at $d_{\text{Nb}} = 0.05$ Å in the left region (corresponding to CDW-1), and the other one is at $d_{\text{Nb}} = 0.07$ Å in the right region (corresponding to CDW-2), confirming that the formation of the Nb trimers stabilizes the

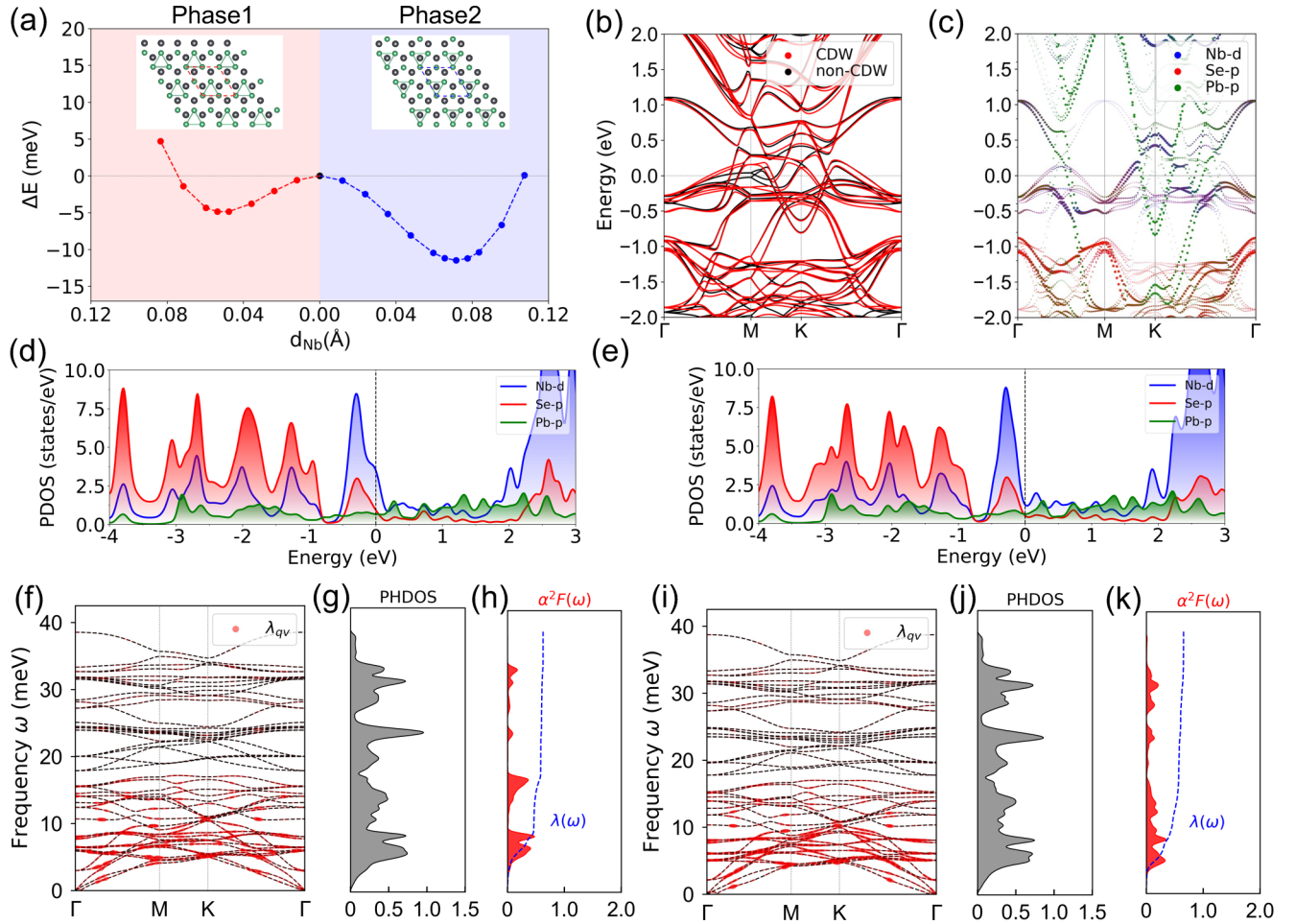


FIG. 6. (a) Relative energy (ΔE) as a function of the atomic displacement in the Nb trimer (d_{Nb}) for the heterobilayer in a 2×2 supercell. The insets show the atomic structures of the charge density wave (CDW)-1 and CDW-2 phases. (b) Band structure of CDW-2 (red line), superimposed by that of the normal phase in the 2×2 Brillouin zone (BZ, black line). (c) Unfolded band structure of CDW-2 in the 1×1 BZ. Projected density of states (PDOS) of the (d) normal and (e) CDW-2 phases. (f) Phonon spectrum of the CDW-2 phase of the heterobilayer calculated without spin-orbit coupling (SOC) and with $\sigma = 0.01$ Ry. The data sizes in red represent the magnitudes of λ_{qv} . (g), (h) The corresponding phonon density of states (PHDOS), Eliashberg function $\alpha^2 F(\omega)$, and accumulative electron-phonon coupling $\lambda(\omega)$ without SOC. (i)–(k) Same as (f)–(h) but with SOC.

2×2 CDW phases. When cooling the system through the CDW transition temperature, the normal phase can settle into either CDW configuration with no barrier. In addition, we also examine two distorted 3×3 superstructures for potential 3×3 CDWs, and the obtained structures are less stable than the 2×2 CDW phases (see Fig. S5 in the Supplemental Material [74]).

Taking CDW-2 as an example, we now investigate the electronic and topological properties of the heterobilayer under the 2×2 CDW modulation. Figure 6(b) displays the band structure of the CDW-2 configuration with SOC, exhibiting obvious band splitting due to the CDW phase transition. To better illustrate the electronic features in the CDW state, we unfold the band structure of the 2×2 supercell into the 1×1 BZ. As shown in Fig. 6(c), the unfolded bands essentially reproduce the main band features of the normal phase [see Fig. 3(c)], except for the gap openings around the M and Γ points ~ 0.4 eV below the Fermi level. Figures 6(d) and 6(e) display the DOS of the normal and CDW phases, respectively,

indicating a significant reduction of the DOS at the Fermi level. Such a feature is induced by the periodic lattice modulation, which helps to stabilize the system. Since the electronic properties of the system are largely preserved in the CDW phase, we expect that the nontrivial topology can also exist after the CDW transition. Indeed, we can identify a curved chemical potential in a continuous gap in the band structure of the CDW phase with SOC (see Fig. S6 in the Supplemental Material [74]). The corresponding Z_2 invariant is evaluated to be 1, suggesting that the CDW system is topologically nontrivial.

Finally, we explore the superconducting properties of the CDW-2 structure and discuss the competition and interplay between CDW and superconductivity. The phonon spectrum of CDW-2 with $\sigma = 0.01$ Ry is presented in Fig. 6(f), where the removal of the imaginary frequencies confirms the dynamic stability of the CDW phase, and the PHDOS, $\alpha^2 F(\omega)$, and $\lambda(\omega)$ for the system are plotted in Figs. 6(g) and 6(h). According to Eq. (3), λ_{qv} depends on the DOS at the Fermi

level available for scattering processes. In addition to the term of $1/N(\varepsilon_F)$, such a dependence is also reflected by the delta functions in Eq. (3). Overall, the total EPC λ can be expressed as approximately proportional to $N(\varepsilon_F)$ [89,90], indicating that the decrease of $N(\varepsilon_F)$ can lead to weaker EPC and smaller $\alpha^2F(\omega)$. As shown in Figs. 6(d) and 6(e), the CDW transition results in an obvious reduction of $N(\varepsilon_F)$ from 0.93 to 0.59 states/eV per 1×1 unit cell, which can qualitatively explain the distinct decrease in the peak value of $\alpha^2F(\omega)$. Meanwhile, the position of the appearance of the peak value is shifted from 2.5 meV in the normal phase to ~ 6.5 meV in the CDW phase [see Figs. 5(g) and 6(h)]. According to Eq. (1), the phonons with higher frequencies will contribute less to the EPC strength due to the weighting of $\alpha^2F(\omega)$ by $1/\omega$. Collectively, the resulting λ is decreased from 3.69 (normal phase) to 0.62 (CDW-2 phase), indicating the coexistence of and competition between CDW and superconductivity in the heterobilayer. Using the Allen-Dynes-modified McMillan equation with $\mu^* = 0.10 - 0.14$, T_c is further estimated to be 2.43–1.56 K, slightly lower than that of monolayered NbSe₂ [78,91]. Therefore, the superconducting property of NbSe₂ can be well preserved when growing a Pb overlayer, even considering the possible CDW phase transition.

Given that SOC has a significant impact on the electronic properties of the heterobilayer and is essential for the emergence of the nontrivial band topology, we further investigate the influence of SOC on the superconducting properties by evaluating the EPC. The phonon spectrum of the CDW-2 phase with SOC is presented in Fig. 6(i), while the corresponding PHDOS, $\alpha^2F(\omega)$, and $\lambda(\omega)$ are plotted in Figs. 6(j) and 6(k). Our findings indicate that SOC has minimal impact on the phonon spectrum and the electron-phonon interaction, showing a very slight softening of the phonons, and the resultant overall λ only increases from 0.62 to 0.65. Notably, according to our electronic property calculations, the DOS at the Fermi level $N(\varepsilon_F)$ exhibits a small increase from 0.59 to 0.62 states/eV per 1×1 unit cell when SOC is considered, which largely accounts for the increase in λ . It is worth noting that the impact of SOC on the EPC in the Pb/NbSe₂ heterobilayer differs significantly from that in bulk Pb, where SOC has a smaller effect on the electronic dispersion relations than Pb/NbSe₂; nevertheless, it substantially increases λ by 44% [92]. By using the Allen-Dynes-modified McMillan equation with $\mu^* = 0.10 - 0.14$, T_c of the heterobilayer with SOC is further estimated to be 2.80–1.86 K. Overall, SOC has no important impact on the superconducting properties. Given that only a heterobilayer system is used to demonstrate the superconducting properties, we expect that, in real systems, the superconductivity can be further enhanced by the proximity effect of the NbSe₂ substrate.

F. Discussion on the realization of TSC

Before closing, we briefly discuss the realization aspect of TSC in our proposed system. As mentioned in Sec. I, the realization of TSC in the Pb/NbSe₂ heterostructures belongs to the reciprocal-space proximity effect scheme [46]. For reciprocal-space proximity-effect-induced TSC, superconductivity arising from bulk bands is proximity coupled to the topologically protected surface/edge states, mimicking

an effective chiral p -wave superconductor. Specifically, the helical edge states are formally equivalent to a superposition of two superconducting states with opposite chirality, which can be gapped out by Cooper pairs. With the presence of time-reversal and particle-hole symmetries, the gapped edge states belong to the DIII class of the tenfold classification and are robust against weak nonmagnetic disorder [93]. It is worthwhile to point out that only when the superconducting electrons flow through the topological edge states do those topological edge states contribute to TSC. As a result, we can obtain helical Majorana fermions. In contrast, the edge states form a topologically trivial phase if gapped by time-reversal symmetry breaking. For the Pb/NbSe₂ heterostructures, the two crucial ingredients of superconductivity and topological edge states are inherently present. Although the topological edge states are located at 0.6 eV below the Fermi level, these states can participate in the superconducting pairing via proper carrier doping or gating, leading to the realization of TSC. To further obtain localized Majorana zero modes, we need to introduce domain walls between the TSC phase and a topologically trivial phase, which can be achieved by attaching a ferromagnetic cluster to the edge [94]. We envision that, for our proposed system, Majorana zero modes can emerge at the ferromagnetic cluster–helical edge state interface.

IV. CONCLUSIONS

To summarize, by employing first-principles approaches, we have identified that a hybrid superconductor of Pb(111)/NbSe₂, consisting of two s -wave superconductors and associated with strong SOC, can exhibit both the nontrivial band topology and superconductivity. The heavy hybridization between Pb and NbSe₂ drives the combined system to endure a topological phase transition, as characterized by the nonzero Z_2 invariant and Dirac cone-type edge states. Here, the SOC induces a gap closure and reopening but without a nontrivial band inversion, suggesting a similar mechanism of topologicalization to that in the Kane-Mele model for graphene. At low temperatures, in contrast with the 3×3 CDW in monolayered NbSe₂, the heterobilayer system has been shown to undergo a 2×2 CDW transition. We have further demonstrated that not only are the nontrivial topological properties inherited in the CDW phase, but the superconductivity is also preserved, although it is weakened due to the blueshifts of the low-frequency phonons and a decrease in $\alpha^2F(\omega)$. In this system, two ingredients of the superconductivity and nontrivial topology are inherently present, making it promising to realize TSC via the reciprocal-space proximity effect. Collectively, our central findings provide an appealing way to realize TSC by constructing a heterostructure from two otherwise conventional s -wave superconductors with strong SOC effects.

ACKNOWLEDGMENTS

This paper was supported in part by the Innovation Program for Quantum Science and Technology (Grant No. 2021ZD0302800), the National Natural Science Foundation of China (Grants No. 11974323 and No. 12374458), the Anhui Initiative in Quantum Information Technologies (Grant

No. AHY170000), the Strategic Priority Research Program of Chinese Academy of Sciences (Grant No. XDB0510200), and

the Anhui Provincial Key Research and Development Project (Grant No. 2023z04020008).

-
- [1] A. Y. Kitaev, Fault-tolerant quantum computation by anyons, *Ann. Phys.* **303**, 2 (2003).
- [2] C. Nayak, S. H. Simon, A. Stern, M. Freedman, and S. Das Sarma, Non-Abelian anyons and topological quantum computation, *Rev. Mod. Phys.* **80**, 1083 (2008).
- [3] F. Wilczek, Majorana returns, *Nat. Phys.* **5**, 614 (2009).
- [4] N. Read and D. Green, Paired states of fermions in two dimensions with breaking of parity and time-reversal symmetries and the fractional quantum Hall effect, *Phys. Rev. B* **61**, 10267 (2000).
- [5] Y. Maeno, H. Hashimoto, K. Yoshida, S. Nishizaki, T. Fujita, J. G. Bednorz, and F. Lichtenberg, Superconductivity in a layered perovskite without copper, *Nature (London)* **372**, 532 (1994).
- [6] A. Pustogow, Y. K. Luo, A. Chronister, Y. S. Su, D. A. Sokolov, F. Jerzembeck, A. P. Mackenzie, C. W. Hicks, N. Kikugawa, S. Raghu *et al.*, Constraints on the superconducting order parameter in Sr_2RuO_4 from oxygen-17 nuclear magnetic resonance, *Nature (London)* **574**, 72 (2019).
- [7] W. Qin, L. Li, and Z. Zhang, Chiral topological superconductivity arising from the interplay of geometric phase and electron correlation, *Nat. Phys.* **15**, 796 (2019).
- [8] S. Ran, C. Eckberg, Q. P. Ding, Y. Furukawa, T. Metz, S. R. Saha, I. L. Liu, M. Zic, H. Kim, J. Paglione *et al.*, Nearly ferromagnetic spin-triplet superconductivity, *Science* **365**, 684 (2019).
- [9] M. Fidrysiak, M. Zegrodnik, and J. Spalek, Unconventional topological superconductivity and phase diagram for an effective two-orbital model as applied to twisted bilayer graphene, *Phys. Rev. B* **98**, 085436 (2018).
- [10] C. Xu and L. Balents, Topological superconductivity in twisted multilayer graphene, *Phys. Rev. Lett.* **121**, 087001 (2018).
- [11] H. Zhou, L. Holleis, Y. Saito, L. Cohen, W. Huynh, C. L. Patterson, F. Yang, T. Taniguchi, K. Watanabe, and A. F. Young, Isospin magnetism and spin-polarized superconductivity in Bernal bilayer graphene, *Science* **375**, 774 (2022).
- [12] W. Qin, C. Huang, T. Wolf, N. Wei, I. Blinov, and A. H. MacDonald, Functional renormalization group study of superconductivity in rhombohedral trilayer graphene, *Phys. Rev. Lett.* **130**, 146001 (2023).
- [13] L. Fu and C. L. Kane, Superconducting proximity effect and Majorana fermions at the surface of a topological insulator, *Phys. Rev. Lett.* **100**, 096407 (2008).
- [14] M. X. Wang, C. H. Liu, J. P. Xu, F. Yang, L. Miao, M. Y. Yao, C. L. Gao, C. Y. Shen, X. C. Ma, X. Chen *et al.*, The coexistence of superconductivity and topological order in the Bi_2Se_3 thin films, *Science* **336**, 52 (2012).
- [15] S.-Y. Xu, N. Alidoust, I. Belopolski, A. Richardella, C. Liu, M. Neupane, G. Bian, S.-H. Huang, R. Sankar, C. Fang *et al.*, Momentum-space imaging of Cooper pairing in a half-Dirac-gas topological superconductor, *Nat. Phys.* **10**, 943 (2014).
- [16] H. H. Sun, M. X. Wang, F. F. Zhu, G. Y. Wang, H. Y. Ma, Z. A. Xu, Q. Liao, Y. H. Lu, C. L. Gao, Y. Y. Li *et al.*, Coexistence of topological edge state and superconductivity in bismuth ultrathin film, *Nano Lett.* **17**, 3035 (2017).
- [17] F. Lüpke, D. Waters, S. C. de la Barrera, M. Widom, D. G. Mandrus, J. Yan, R. M. Feenstra, and B. M. Hunt, Proximity-induced superconducting gap in the quantum spin Hall edge state of monolayer WTe_2 , *Nat. Phys.* **16**, 526 (2020).
- [18] J.-P. Xu, M.-X. Wang, Z. L. Liu, J.-F. Ge, X. Yang, C. Liu, Z. A. Xu, D. Guan, C. L. Gao, D. Qian *et al.*, Experimental detection of a Majorana mode in the core of a magnetic vortex inside a topological insulator-superconductor $\text{Bi}_2\text{Te}_3/\text{NbSe}_2$ Heterostructure, *Phys. Rev. Lett.* **114**, 017001 (2015).
- [19] Y. S. Hor, A. J. Williams, J. G. Checkelsky, P. Roushan, J. Seo, Q. Xu, H. W. Zandbergen, A. Yazdani, N. P. Ong, and R. J. Cava, Superconductivity in $\text{Cu}_x\text{Bi}_2\text{Se}_3$ and its implications for pairing in the undoped topological insulator, *Phys. Rev. Lett.* **104**, 057001 (2010).
- [20] Z. Liu, X. Yao, J. Shao, M. Zuo, L. Pi, S. Tan, C. Zhang, and Y. Zhang, Superconductivity with topological surface state in $\text{Sr}_x\text{Bi}_2\text{Se}_3$, *J. Am. Chem. Soc.* **137**, 10512 (2015).
- [21] L. A. Wray, S.-Y. Xu, Y. Xia, Y. S. Hor, D. Qian, A. V. Fedorov, H. Lin, A. Bansil, R. J. Cava, and M. Z. Hasan, Observation of topological order in a superconducting doped topological insulator, *Nat. Phys.* **6**, 855 (2010).
- [22] J. X. Yin, Z. Wu, J. H. Wang, Z. Y. Ye, J. Gong, X. Y. Hou, L. Shan, A. Li, X. J. Liang, X. X. Wu *et al.*, Observation of a robust zero-energy bound state in iron-based superconductor $\text{Fe}(\text{Te},\text{Se})$, *Nat. Phys.* **11**, 543 (2015).
- [23] Z. Wang, P. Zhang, G. Xu, L. K. Zeng, H. Miao, X. Xu, T. Qian, H. Weng, P. Richard, A. V. Fedorov *et al.*, Topological nature of the $\text{FeSe}_{0.5}\text{Te}_{0.5}$ superconductor, *Phys. Rev. B* **92**, 115119 (2015).
- [24] G. Xu, B. Lian, P. Tang, X.-L. Qi, and S.-C. Zhang, Topological superconductivity on the surface of Fe-based superconductors, *Phys. Rev. Lett.* **117**, 047001 (2016).
- [25] P. Zhang, K. Yaji, T. Hashimoto, Y. Ota, T. Kondo, K. Okazaki, Z. Wang, J. Wen, G. D. Gu, H. Ding *et al.*, Observation of topological superconductivity on the surface of an iron-based superconductor, *Science* **360**, 182 (2018).
- [26] P. Zhang, Z. Wang, X. Wu, K. Yaji, Y. Ishida, Y. Kohama, G. Dai, Y. Sun, C. Bareille, K. Kuroda *et al.*, Multiple topological states in iron-based superconductors, *Nat. Phys.* **15**, 41 (2019).
- [27] L. Kong, S. Zhu, M. Papaj, H. Chen, L. Cao, H. Isobe, Y. Xing, W. Liu, D. Wang, P. Fan *et al.*, Half-integer level shift of vortex bound states in an iron-based superconductor, *Nat. Phys.* **15**, 1181 (2019).
- [28] P. Fan, F. Yang, G. Qian, H. Chen, Y.-Y. Zhang, G. Li, Z. Huang, Y. Xing, L. Kong, W. Liu *et al.*, Observation of magnetic adatom-induced Majorana vortex and its hybridization with field-induced Majorana vortex in an iron-based superconductor, *Nat. Commun.* **12**, 1348 (2021).
- [29] T.-R. Chang, P.-J. Chen, G. Bian, S.-M. Huang, H. Zheng, T. Neupert, R. Sankar, S.-Y. Xu, I. Belopolski, G. Chang *et al.*, Topological Dirac surface states and superconducting pairing correlations in PbTaSe_2 , *Phys. Rev. B* **93**, 245130 (2016).
- [30] Z. Sun, M. Enayat, A. Maldonado, C. Lithgow, E. Yelland, D. C. Peets, A. Yaresko, A. P. Schnyder, and P. Wahl, Dirac

- surface states and nature of superconductivity in noncentrosymmetric BiPd, *Nat. Commun.* **6**, 6633 (2015).
- [31] L. Li, S. Zhang, G. Hu, L. Guo, T. Wei, W. Qin, B. Xiang, C. Zeng, Z. Zhang, and P. Cui, Converting a monolayered NbSe₂ into an Ising superconductor with nontrivial band topology via physical or chemical pressuring, *Nano Lett.* **22**, 6767 (2022).
- [32] J. Gao, W. Ding, S. Zhang, Z. Zhang, and P. Cui, Coexistence of superconductivity and nontrivial band topology in monolayered cobalt pnictides on SrTiO₃, *Nano Lett.* **21**, 7396 (2021).
- [33] Z. Fei, T. Palomaki, S. Wu, W. Zhao, X. Cai, B. Sun, P. Nguyen, J. Finney, X. Xu, and D. H. Cobden, Edge conduction in monolayer WTe₂, *Nat. Phys.* **13**, 677 (2017).
- [34] S. Tang, C. Zhang, D. Wong, Z. Pedramrazi, H.-Z. Tsai, C. Jia, B. Moritz, M. Claassen, H. Ryu, S. Kahn *et al.*, Quantum spin Hall state in monolayer 1T'-WTe₂, *Nat. Phys.* **13**, 683 (2017).
- [35] V. Fatemi, S. Wu, Y. Cao, L. Bretheau, Q. D. Gibson, K. Watanabe, T. Taniguchi, R. J. Cava, and P. Jarillo-Herrero, Electrically tunable low-density superconductivity in a monolayer topological insulator, *Science* **362**, 926 (2018).
- [36] E. Sajadi, T. Palomaki, Z. Fei, W. Zhao, P. Bement, C. Olsen, S. Luescher, X. Xu, J. A. Folk, and D. H. Cobden, Gate-induced superconductivity in a monolayer topological insulator, *Science* **362**, 922 (2018).
- [37] J.-Y. You, B. Gu, G. Su, and Y. P. Feng, Two-dimensional topological superconductivity candidate in a van der Waals layered material, *Phys. Rev. B* **103**, 104503 (2021).
- [38] J. Chen and Y. Ge, Emergence of intrinsic superconductivity in monolayer W₂N₃, *Phys. Rev. B* **103**, 064510 (2021).
- [39] D. Campi, S. Kumari, and N. Marzari, Prediction of phonon-mediated superconductivity with high critical temperature in the two-dimensional topological semimetal W₂N₃, *Nano Lett.* **21**, 3435 (2021).
- [40] M. Liao, Y. Zang, Z. Guan, H. Li, Y. Gong, K. Zhu, X.-P. Hu, D. Zhang, Y. Xu, Y.-Y. Wang *et al.*, Superconductivity in few-layer stanene, *Nat. Phys.* **14**, 344 (2018).
- [41] C. Zhao, L. Li, L. Zhang, J. Qin, H. Chen, B. Xia, B. Yang, H. Zheng, S. Wang, C. Liu *et al.*, Coexistence of robust edge states and superconductivity in few-layer stanene, *Phys. Rev. Lett.* **128**, 206802 (2022).
- [42] J. Y. Chen, W. Qin, P. Cui, and Z. Y. Zhang, Enhanced stability and superconductivity of IrTe₂/In₂Se₃ heterobilayers with ferroelectrically switchable band topology, *Phys. Rev. B* **108**, 085408 (2023).
- [43] J. Y. Chen, W. Qin, P. Cui, and Z. Y. Zhang, Ferroelectric tuning of superconductivity and band topology in a two-dimensional heterobilayer, *Phys. Rev. B* **108**, L060501 (2023).
- [44] Y. T. Yang, W. Qin, Y. R. Chen, S. H. Zhang, P. Cui, and Z. Y. Zhang, Endowing Ising superconductor NbSe₂ with nontrivial band topology via proximity coupling with two-dimensional ferromagnet Fe₃GeTe₂, *Phys. Rev. B* **109**, L041112 (2024).
- [45] J. Q. Gao, Z. Y. Zhang, and P. Cui, Topological and superconducting properties of monolayered CoN and CoP: A first-principles comparative study, *Sci. China-Phys. Mech. Astron.* **67**, 257011 (2024).
- [46] W. Qin, J. Gao, P. Cui, and Z. Zhang, Two-dimensional superconductors with intrinsic *p*-wave pairing or nontrivial band topology, *Sci. China-Phys. Mech. Astron.* **66**, 267005 (2023).
- [47] C. L. Kane and E. J. Mele, Quantum spin Hall effect in graphene, *Phys. Rev. Lett.* **95**, 226801 (2005).
- [48] C. L. Kane and E. J. Mele, Z₂ topological order and the quantum spin Hall effect, *Phys. Rev. Lett.* **95**, 146802 (2005).
- [49] B. A. Bernevig, T. L. Hughes, and S.-C. Zhang, Quantum spin Hall effect and topological phase transition in HgTe quantum wells, *Science* **314**, 1757 (2006).
- [50] J. H. Dil, F. Meier, J. Lobo-Checa, L. Patthey, G. Bihlmayer, and J. Osterwalder, Rashba-type spin-orbit splitting of quantum well states in ultrathin Pb films, *Phys. Rev. Lett.* **101**, 266802 (2008).
- [51] K. Yaji, Y. Ohtsubo, S. Hatta, H. Okuyama, K. Miyamoto, T. Okuda, A. Kimura, H. Namatame, M. Taniguchi, and T. Aruga, Large Rashba spin splitting of a metallic surface-state band on a semiconductor surface, *Nat. Commun.* **1**, 17 (2010).
- [52] S. Y. Qin, J. Kim, Q. Niu, and C. K. Shih, Superconductivity at the two-dimensional limit, *Science* **324**, 1314 (2009).
- [53] T. Zhang, P. Cheng, W.-J. Li, Y.-J. Sun, G. Wang, X.-G. Zhu, K. He, L. Wang, X. Ma, X. Chen *et al.*, Superconductivity in one-atomic-layer metal films grown on Si(111), *Nat. Phys.* **6**, 104 (2010).
- [54] G. Kresse and J. Hafner, *Ab initio* molecular dynamics for open-shell transition metals, *Phys. Rev. B* **48**, 13115 (1993).
- [55] G. Kresse and J. Furthmüller, Efficient iterative schemes for *ab initio* total-energy calculations using a plane-wave basis set, *Phys. Rev. B* **54**, 11169 (1996).
- [56] P. E. Blöchl, Projector augmented-wave method, *Phys. Rev. B* **50**, 17953 (1994).
- [57] G. Kresse and D. Joubert, From ultrasoft pseudopotentials to the projector augmented-wave method, *Phys. Rev. B* **59**, 1758 (1999).
- [58] J. P. Perdew, K. Burke, and M. Ernzerhof, Generalized gradient approximation made simple, *Phys. Rev. Lett.* **77**, 3865 (1996).
- [59] S. Nosé, A unified formulation of the constant temperature molecular dynamics methods, *J. Chem. Phys.* **81**, 511 (1984).
- [60] A. A. Soluyanov and D. Vanderbilt, Computing topological invariants without inversion symmetry, *Phys. Rev. B* **83**, 235401 (2011).
- [61] M. P. L. Sancho, J. M. L. Sancho, J. M. L. Sancho, and J. Rubio, Highly convergent schemes for the calculation of bulk and surface Green functions, *J. Phys. F* **15**, 851 (1985).
- [62] A. A. Mostofi, J. R. Yates, Y.-S. Lee, I. Souza, D. Vanderbilt, and N. Marzari, WANNI90: A tool for obtaining maximally-localised Wannier functions, *Comput. Phys. Commun.* **178**, 685 (2008).
- [63] Q. Wu, S. Zhang, H.-F. Song, M. Troyer, and A. A. Soluyanov, WANNIERTOOLS: An open-source software package for novel topological materials, *Comput. Phys. Commun.* **224**, 405 (2018).
- [64] S. Grimme, Semiempirical GGA-type density functional constructed with a long-range dispersion correction, *Comput. Chem.* **27**, 1787 (2006).
- [65] S. Grimme, J. Antony, S. Ehrlich, and H. Krieg, A consistent and accurate *ab initio* parametrization of density functional dispersion correction (DFT-D) for the 94 elements H-Pu, *J. Chem. Phys.* **132**, 154104 (2010).
- [66] K. Lee, É. D. Murray, L. Kong, B. I. Lundqvist, and D. C. Langreth, Higher-accuracy van der Waals density functional, *Phys. Rev. B* **82**, 081101(R) (2010).
- [67] J. Klimeš, D. R. Bowler, and A. Michaelides, Chemical accuracy for the van der Waals density functional, *J. Phys.* **22**, 022201 (2009).

- [68] A. Meerschaut and C. Deudon, Crystal structure studies of the $3R\text{-Nb}_{1.09}\text{S}_2$ and the $2H\text{-NbSe}_2$ compounds: Correlation between nonstoichiometry and stacking type (=polytypism), *Mater. Res. Bull.* **36**, 1721 (2001).
- [69] P. Giannozzi, S. Baroni, N. Bonini, M. Calandra, R. Car, C. Cavazzoni, D. Ceresoli, G. L. Chiarotti, M. Cococcioni, I. Dabo *et al.*, QUANTUM ESPRESSO: A modular and open-source software project for quantum simulations of materials, *J. Phys.: Condens. Matter* **21**, 395502 (2009).
- [70] D. R. Hamann, Optimized norm-conserving Vanderbilt pseudopotentials, *Phys. Rev. B* **88**, 085117 (2013).
- [71] F. Giustino, M. L. Cohen, and S. G. Louie, Electron-phonon interaction using Wannier functions, *Phys. Rev. B* **76**, 165108 (2007).
- [72] S. Ponc e, E. R. Margine, C. Verdi, and F. Giustino, EPW: Electron-phonon coupling, transport and superconducting properties using maximally localized Wannier functions, *Comput. Phys. Commun.* **209**, 116 (2016).
- [73] A. Franceschetti, Structural and electronic properties of PbSe nanocrystals from first principles, *Phys. Rev. B* **78**, 075418 (2008).
- [74] See Supplemental Material at <http://link.aps.org/supplemental/10.1103/PhysRevB.109.224516> for the band structures of four-layer NbSe₂, Wannier charge centers for different Pb(111)/NbSe₂ systems, orbital contributions of valence and conduction bands in the whole BZ, atomic structures of distorted heterobilayers, and topological properties of the CDW-2 phase.
- [75] S. Kezilebieke, M. N. Huda, V. Va no, M. Aapro, S. C. Ganguli, O. J. Silveira, S. G odzik, A. S. Foster, T. Ojanen, and P. Liljeroth, Topological superconductivity in a van der Waals heterostructure, *Nature (London)* **588**, 424 (2020).
- [76] Y. Xia, D. Qian, D. Hsieh, L. Wray, A. Pal, H. Lin, A. Bansil, D. Grauer, Y. S. Hor, R. J. Cava *et al.*, Observation of a large-gap topological-insulator class with a single Dirac cone on the surface, *Nat. Phys.* **5**, 398 (2009).
- [77] F. Weber, L. Pintschovius, W. Reichardt, R. Heid, K. P. Bohnen, A. Kreyssig, D. Reznik, and K. Hradil, Phonons and electron-phonon coupling in YNi₂B₂C, *Phys. Rev. B* **89**, 104503 (2014).
- [78] X. Xi, L. Zhao, Z. Wang, H. Berger, L. Forr o, J. Shan, and K. F. Mak, Strongly enhanced charge-density-wave order in monolayer NbSe₂, *Nat. Nanotechnol.* **10**, 765 (2015).
- [79] O. R. Albertini, A. Y. Liu, and M. Calandra, Effect of electron doping on lattice instabilities in single-layer $1H\text{-TaS}_2$, *Phys. Rev. B* **95**, 235121 (2017).
- [80] Y. Chen, L. S. Wu, H. Xu, C. X. Cong, S. Li, S. Feng, H. B. Zhang, C. J. Zou, J. Z. Shang *et al.*, Visualizing the anomalous charge density wave states in graphene/NbSe₂ heterostructures, *Adv. Mater.* **32**, 2003746 (2020).
- [81] S. Cahangirov, M. Topsakal, E. Akt urk, H. Sahin, and S. Ciraci, Two- and one-dimensional honeycomb structures of silicon and germanium, *Phys. Rev. Lett.* **102**, 236804 (2009).
- [82] H. Sahin, S. Cahangirov, M. Topsakal, E. Bekaroglu, E. Akturk, R. T. Senger, and S. Ciraci, Monolayer honeycomb structures of group-IV elements and III-V binary compounds: First-principles calculations, *Phys. Rev. B* **80**, 155453 (2009).
- [83] W. L. McMillan, Transition temperature of strong-coupled superconductors, *Phys. Rev.* **167**, 331 (1968).
- [84] P. B. Allen and R. C. Dynes, Transition temperature of strong-coupled superconductors reanalyzed, *Phys. Rev. B* **12**, 905 (1975).
- [85] J. Noffsinger and M. L. Cohen, Superconductivity in monolayer Pb on Si(111) from first principles, *Solid State Commun.* **151**, 421 (2011).
- [86] I. Y. Sklyadneva, R. Heid, K. P. Bohnen, P. M. Echenique, and E. V. Chulkov, Electron-phonon coupling and superconductivity in the (4/3)-monolayer of Pb on Si(111): Role of spin-orbit interaction, *Phys. Rev. B* **97**, 195409 (2018).
- [87] F. Zheng and J. Feng, Electron-phonon coupling and the coexistence of superconductivity and charge-density wave in monolayer NbSe₂, *Phys. Rev. B* **99**, 161119(R) (2019).
- [88] H. Tan, Y. Liu, Z. Wang, and B. Yan, Charge density waves and electronic properties of superconducting kagome metals, *Phys. Rev. Lett.* **127**, 046401 (2021).
- [89] S. Blackburn, M. C ot e, S. G. Louie, and M. L. Cohen, Enhanced electron-phonon coupling near the lattice instability of superconducting NbC_{1-x}N_x from density-functional calculations, *Phys. Rev. B* **84**, 104506 (2011).
- [90] G. Profeta, M. Calandra, and F. Mauri, Phonon-mediated superconductivity in graphene by lithium deposition, *Nat. Phys.* **8**, 131 (2012).
- [91] M. M. Ugeda, A. J. Bradley, Y. Zhang, S. Onishi, Y. Chen, W. Ruan, C. Ojeda-Aristizabal, H. Ryu, M. T. Edmonds, H.-Z. Tsai *et al.*, Characterization of collective ground states in single-layer NbSe₂, *Nat. Phys.* **12**, 92 (2016).
- [92] R. Heid, K. P. Bohnen, I. Y. Sklyadneva, and E. V. Chulkov, Effect of spin-orbit coupling on the electron-phonon interaction of the superconductors Pb and Tl, *Phys. Rev. B* **81**, 174527 (2010).
- [93] A. P. Schnyder, S. Ryu, A. Furusaki, and A. W. W. Ludwig, Classification of topological insulators and superconductors in three spatial dimensions, *Phys. Rev. B* **78**, 195125 (2008).
- [94] B. J ack, Y. L. Xie, J. Li, S. Jeon, B. A. Bernevig, and A. Yazdani, Observation of a Majorana zero mode in a topologically protected edge channel, *Science* **364**, 1255 (2019).